

DISN: Deep Implicit Surface Network for High-quality Single-view 3D Reconstruction

Weiyue Wang^{*,1}Qiangeng Xu^{*,1}Duygu Ceylan²Radomir Mech²Ulrich Neumann¹¹University of Southern California
Los Angeles, California²Adobe

San Jose, California

{weiyuewa, qiangenx, uneumann}@usc.edu

{ceylan, rmech}@adobe.com

Abstract

Reconstructing 3D shapes from single-view images has been a long-standing research problem and has attracted a lot of attention. In this paper, we present *DISN*, a Deep Implicit Surface Network that generates a high-quality 3D shape given an input image by predicting the underlying signed distance field. In addition to utilizing global image features, DISN also predicts the local image patch each 3D point sample projects onto and extracts local features from the patch. Combining global and local features significantly improves the accuracy of the predicted signed distance field. To the best of our knowledge, DISN is the first method that constantly captures details such as holes and thin structures present in 3D shapes from single-view images. DISN achieves state-of-the-art single-view reconstruction performance on a variety of shape categories reconstructed from both synthetic and real images. Code is available at github.com/laughtervv/DISN.

1 Introduction

Over the recent years, a multitude of single-view 3D reconstruction methods have been proposed where deep learning based methods have specifically achieved promising results. To represent 3D shapes, many of these methods utilize either voxels [28, 6, 31, 25, 20, 26, 29, 24] or point clouds [5] due to ease of encoding them in a neural network. However, such representations are often limited in terms of resolution. A few recent methods have explored utilizing explicit surface representations, i.e., polygonal meshes, in a neural network but make the assumption of a fixed topology [7, 21, 23] limiting the flexibility of the approaches. Moreover, point- and mesh-based methods use Chamfer Distance (CD) and Earthmover Distance (EMD) as training losses. However, these distances provide only approximated metrics for measuring shape similarity.

To address the aforementioned limitations in voxels, point clouds and meshes, in this paper, we study an alternative implicit 3D surface representation, Signed Distance Functions (SDF). We present an

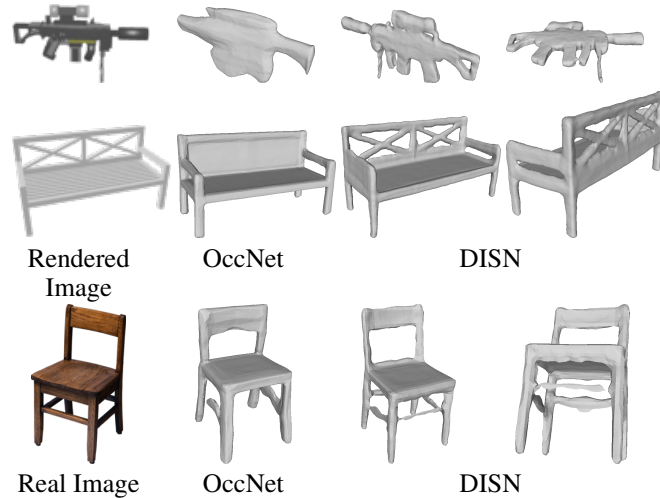


Figure 1: Single-view reconstruction results using OccNet [12], a state-of-the-art method, and DISN on synthetic and real images.

* indicates equal contributions.

efficient, flexible, and effective Deep Implicit Surface Network (DISN) for predicting SDFs from single-view images (Figure 1). SDF simply encodes the signed distance of each point sample in 3D from the boundary of the underlying shape. Thus, given a set of signed distance values, the shape can be extracted by identifying the iso-surface using methods such as *Marching Cubes* [11]. As illustrated in Figure 3, given a convolutional neural network (CNN) that encodes the input image into a feature vector, DISN predicts the SDF value of a given 3D point using this feature vector. By sampling different 3D point locations, DISN is able to generate an implicit field of the underlying surface with infinite resolution. Moreover, without the need of a fixed topology assumption, the regressing target for DISN is an accurate ground truth instead of an approximated metric.

While many single-view 3D reconstruction methods [28, 5, 2, 12] that learn a shape embedding from a 2D image are able to capture the global shape properties, they have a tendency to ignore details such as holes or thin structures, resulting in visually unsatisfactory reconstruction. To address this problem, we further introduce a local feature extraction module. Specifically, we estimate the viewpoint parameters of the input image. We utilize this information to project each query point onto the input image to identify a corresponding local patch. We extract local features from such patches and use them in conjunction with global image features to predict the SDF value of the points. This module enables the network to learn the relations between projected pixels and 3D space, and significantly improves the reconstruction quality of fine-grained details in the resulting 3D shape. As shown in Figure 1, DISN is able to generate shape details, such as the patterns on the bench back and holes on the rifle handle, which previous state-of-the-art methods fail to produce. To the best of our knowledge, DISN is the first deep learning model that is able to capture such high-quality details from single-view images.

We evaluate our approach on various shape categories using both synthetic data generated from 3D shape datasets as well as online product images. Qualitative and quantitative comparisons demonstrate that our network outperforms state-of-the-art methods and generates plausible shapes with high-quality details. Furthermore, we also extend DISN to multi-view reconstruction and other applications such as shape interpolation.

2 Related Work

Over the last few years, there have been extensive studies on learning based single-view 3D reconstruction using various 3D representations including voxels [28, 6, 31, 25, 20, 26, 29], octrees [8, 19, 22], points [5], and primitives [32, 13]. More recently, Sinha et al. [17] propose a method to generate the surface of an object using geometry images. Tang et al. [18] use shape skeletons for surface reconstruction, however, their method requires additional shape primitives dataset. Groueix et al. [7] present AtlasNet to generate surfaces of 3D shapes using a set of parametric surface elements. Wang et al. [21] introduce a graph-based network Pix2Mesh to reconstruct 3D manifold shapes from input images whereas Wang et al. [23] present 3DN to reconstruct a 3D shape by deforming a given source mesh.

Most of the aforementioned methods use explicit 3D representations and often suffer from problems such as limited resolution and fixed mesh topology. Implicit representations provide an alternative representation to overcome these limitations. In our work, we adopt the Signed Distance Functions (SDF) which are among the most popular implicit surface representations. Several deep learning approaches have utilized SDFs recently. Dai et al. [4] use a voxel-based SDF representation for shape inpainting. Nevertheless, the 3D CNNs are known to suffer from high memory usage and computation cost. Park et al. [14] introduce DeepSDF for shape completion using an auto-decoder structure. However, their network is not feed-forward and requires optimizing the embedding vector during test time which limits the efficiency and capability of the approach. In concurrent work, Chen and Zhang [2] use SDFs in deep networks for the task of shape generation. While their method achieves promising results for the generation task, it fails to recover fine-grained details of 3D objects for single-view reconstruction. Finally, Mescheder et al. [12] learn an implicit representation by predicting the probability of each cell in a volumetric grid being occupied or not, i.e., being inside or outside of a 3D model. By iteratively subdividing each active cell (i.e., cells surrounded by occupied and empty cells) into sub-cells and repeating the prediction for each sub-cell, they alleviate the problem of limited resolution of volumetric grids. In contrast, our method not only predicts the sign (i.e., being inside or outside) of sampled points but also the distance which is continuous. Therefore, an iterative prediction procedure is not necessary. We compare our method with these recent approaches in Section 4.1 and demonstrate state-of-the-art results.

3 Method

Given an image of an object, our goal is to reconstruct a 3D shape that captures both the overall structure and fine-grained details of the object. We consider modeling a 3D shape as a signed distance function (SDF). As illustrated in Figure 2, SDF is a continuous function that maps a given spatial point $\mathbf{p} = (x, y, z) \in \mathbb{R}^3$ to a real value $s \in \mathbb{R}$: $s = SDF(\mathbf{p})$. The absolute value of s indicates the distance of the point to the surface, while the sign of s represents if the point is inside or outside the surface. An iso-surface $\mathcal{S}_0 = \{\mathbf{p} | SDF(\mathbf{p}) = 0\}$ implicitly represents the underlying 3D shape.

In this paper, we use a feed-forward deep neural network, Deep Implicit Surface Network (DISN), to predict the SDF from an input image. DISN takes a single image as input and predicts the SDF value for any given point. Unlike the 3D CNN methods [4] which generate a volumetric grid with fixed resolution, DISN produces a continuous field with arbitrary resolution. Moreover, we introduce a local feature extraction method to improve recovery of shape details.

3.1 DISN: Deep Implicit Surface Network

The overview of our method is illustrated in Figure 3. Given an image, DISN consists of two parts: *camera pose estimation* and *SDF prediction*. DISN first estimates the camera parameters that map an object in world coordinates to the image plane. Given the predicted camera parameters, we project each 3D query point onto the image plane and collect multi-scale CNN features for the corresponding image patch. DISN then decodes the given spatial point to an SDF value using both the multi-scale local image features and the global image features.

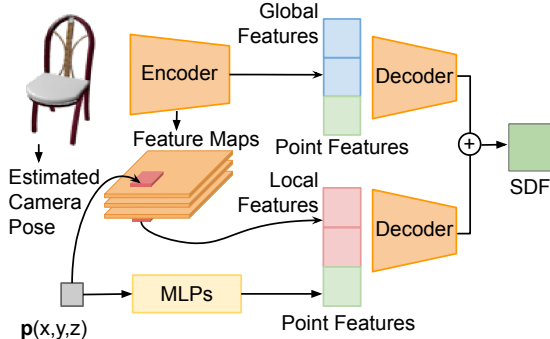


Figure 3: Given an image and a point \mathbf{p} , we estimate the camera pose and project \mathbf{p} onto the image plane. DISN uses the local features at the projected location, the global features, and the point features to predict the SDF of \mathbf{p} . ‘MLPs’ denotes multi-layer perceptrons.

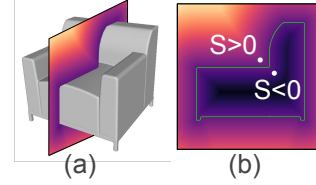


Figure 2: Illustration of SDF. (a) Rendered 3D surface with $s = 0$. (b) Cross-section of the SDF. A point is outside the surface if $s > 0$, inside if $s < 0$, and on the surface if $s = 0$.

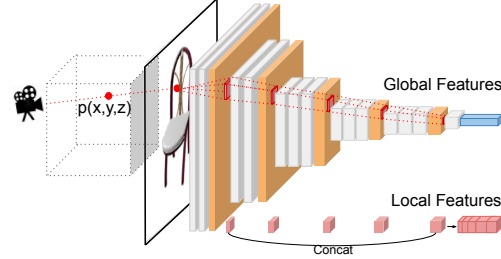


Figure 4: Local feature extraction. Given a 3D point \mathbf{p} , we use the estimated camera parameters to project \mathbf{p} onto the image plane. Then we identify the projected location on each feature map layer of the encoder. We concatenate features at each layer to get the local features of point \mathbf{p} .

3.1.1 Camera Pose Estimation

Given an input image, our first goal is to estimate the corresponding viewpoint. We train our network on the ShapeNet Core dataset [1] where all the models are aligned. Therefore we use this aligned model space as the world space where our camera parameters are with respect to, and we assume a fixed set of intrinsic parameters. Regressing camera parameters from an input image directly using a CNN often fails to produce accurate poses as discussed in [9]. To overcome this issue, Insafutdinov and Dosovitskiy [9] introduce a distilled ensemble approach to regress camera pose by combining several pose candidates. However, this method requires a large number of network parameters and a complex training procedure. We present a more efficient and effective network illustrated in Figure 5. In a recent work, Zhou et al. [30] show that a 6D rotation representation is continuous and easier for a neural network to regress compared to more commonly used representations such as quaternions and Euler angles. Thus, we employ the 6D rotation representation $\mathbf{b} = (\mathbf{b}_x, \mathbf{b}_y)$, where $\mathbf{b} \in \mathbb{R}^6, \mathbf{b}_x \in \mathbb{R}^3, \mathbf{b}_y \in \mathbb{R}^3$. Given \mathbf{b} , the rotation matrix $\mathbf{R} = (\mathbf{R}_x, \mathbf{R}_y, \mathbf{R}_z)^T \in \mathbb{R}^{3 \times 3}$ is obtained by

$$\mathbf{R}_x = N(\mathbf{b}_x), \mathbf{R}_z = N(\mathbf{R}_x \times \mathbf{b}_y), \mathbf{R}_y = \mathbf{R}_z \times \mathbf{R}_x, \quad (1)$$

where $\mathbf{R}_x, \mathbf{R}_y, \mathbf{R}_z \in \mathbb{R}^3$, $N(\cdot)$ is the normalization function, ‘ \times ’ indicates cross product. Translation $\mathbf{t} \in \mathbb{R}^3$ from world space to camera space is directly predicted by the network.

Instead of calculating losses on camera parameters directly as in [9], we use the predicted camera pose to transform a given point cloud from the world space to the camera coordinate space. We compute the loss L_{cam} by calculating the mean squared error between the transformed point cloud and the ground truth point cloud in the camera space:

$$L_{cam} = \frac{\sum_{\mathbf{p}_w \in PC_w} \|\mathbf{p}_G - (\mathbf{R}\mathbf{p}_w + \mathbf{t})\|_2^2}{\sum_{\mathbf{p}_w \in PC_w} 1}, \quad (2)$$

where $PC_w \in \mathbb{R}^{N \times 3}$ is the point cloud in the world space, N is number of points in PC_w . For each $\mathbf{p}_w \in PC_w$, \mathbf{p}_G represents the corresponding ground truth point location in the camera space and $\|\cdot\|_2^2$ is the squared L_2 distance.

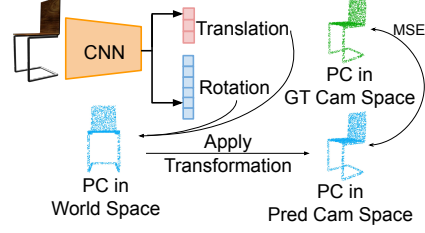


Figure 5: Camera Pose Estimation Network. ‘PC’ denotes point cloud. ‘GT Cam’ and ‘Pred Cam’ denote the ground truth and predicted cameras.

3.1.2 SDF Prediction with Deep Neural Network

Given an image I , we denote the groundtruth SDF by $SDF^I(\cdot)$, and the goal of our network $f(\cdot)$ is to estimate $SDF^I(\cdot)$. Unlike the common used CD and EMD losses in previous reconstruction methods [5, 7], our guidance is a true ground truth instead of approximated metrics.

Park et al [14] recently propose DeepSDF, a direct approach to regress SDF with a neural network. DeepSDF concatenates the location of a query 3D point and the shape embedding extracted from a depth image or a point cloud and uses an auto-decoder to obtain the corresponding SDF value. The auto-decoder structure requires optimizing the shape embedding for each object. In our initial experiments, when we applied a similar network architecture in a feed-forward manner, we observed convergence issues. Alternatively, Chen and Zhang [2] propose to concatenate the global features of an input image and the location of a query point to every layer of a decoder. While this approach works better in practice, it also results in a significant increase in the number of network parameters. Our solution is to use a multi-layer perceptron to map the given point location to a higher-dimensional feature space. This high dimensional feature is then concatenated with global and local image features respectively and used to regress the SDF value. We provide the details of our network in the supplementary.

Local Feature Extraction As shown in Figure 6(a), our initial experiments showed that it is hard to capture shape details such as holes and thin structures when only global image features are used. Thus, we introduce a local feature extraction method to focus on reconstructing fine-grained details, such as the back poles of a chair (Figure 6). As illustrated in Figure 4, a 3D point $\mathbf{p} \in \mathbb{R}^3$ is projected to a 2D location $\mathbf{q} \in \mathbb{R}^2$ on the image plane with the estimated camera parameters. We retrieve features on each feature map corresponding to location \mathbf{q} and concatenate them to get the local image features. Since the feature maps in the later layers are smaller in dimension than the original image, we resize them to the original size with bilinear interpolation and extract the resized features at location \mathbf{q} .

Two decoders then take the global and local image features respectively as input with the point features and make an SDF prediction. The final SDF is the sum of these two predictions. Figure 6 compares the results of our approach with and without local feature extraction. With only global features, the network is able to predict the overall shape but fails to produce details. Local feature extraction helps to recover these missing details by predicting the *residual* SDF.

Loss Functions We regress continuous SDF values instead of formulating a binary classification problem (e.g., inside or outside of a shape) as in [2]. This strategy enables us to extract surfaces that correspond to different iso-values. To ensure that the network concentrates on recovering the details near and inside the iso-surface S_0 , we propose a weighted loss function. Our loss is defined by



Figure 6: Shape reconstruction results (a) without and (b) with local feature extraction.

$$L_{SDF} = \sum_{\mathbf{p}} m |f(I, \mathbf{p}) - SDF^I(\mathbf{p})|, \quad (3)$$

$$m = \begin{cases} m_1, & \text{if } SDF^I(\mathbf{p}) < \delta, \\ m_2, & \text{otherwise,} \end{cases}$$

where $|\cdot|$ is the L_1 -norm. m_1, m_2 are different weights, and for points whose signed distance is below a certain threshold δ , we use a higher weight of m_1 .

3.2 Surface Reconstruction

To generate a mesh surface, we firstly define a dense 3D grid and predict SDF values for each grid point. Once we compute the SDF values for each point in the dense grid, we use Marching Cubes [11] to obtain the 3D mesh that corresponds to the iso-surface \mathcal{S}_0 .

4 Experiments

We perform quantitative and qualitative comparisons on single-view 3D reconstruction with state-of-the-art methods [7, 21, 23, 2, 12] in Section 4.1. We also compare the performance of our method on camera pose estimation with [9] in Section 4.2. We further conduct ablation studies in Section 4.3 and showcase several applications in Section 4.4. More qualitative results and all detailed network architectures can be found in the supplementary.

Dataset For both camera prediction and SDF prediction, we follow the settings of [7, 21, 23, 12], and use the ShapeNet Core dataset [1], which includes 13 object categories, and an official training/testing split to train and test our method. For 2D images, we use the rendered views provided by Choy et al [3]. We train a single network on all categories and report the test results generated by this network.

Data Preparation and Implementation Details For each 3D mesh in ShapeNet Core, we first generate an SDF grid with resolution 256^3 using [27, 16]. Models in ShapeNet Core are aligned and

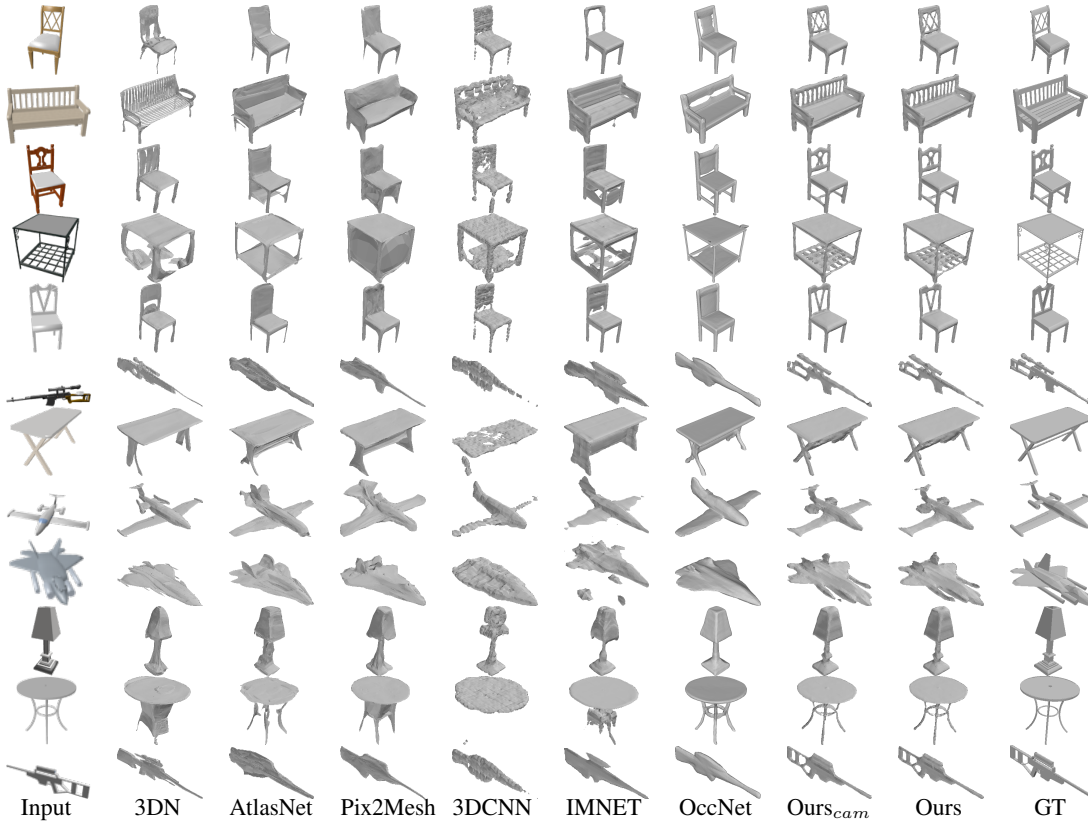


Figure 7: Single-view reconstruction results of various methods. ‘GT’ denotes ground truth shapes. Best viewed on screen with zooming in.

we choose this aligned model space as our world space where each render view in [3] represents a transformation to a different camera space.

We train our camera pose estimation network and SDF prediction network separately. For both networks, we use VGG-16 [15] as the image encoder. When training the SDF prediction network, we extract the local features using the ground truth camera parameters. As mentioned in Section 3.1, DISN is able to generate a signed distance field with arbitrary resolution by continuously sampling points and regressing their SDF values. However, in practice, we are interested in points near the iso-surface S_0 . Therefore, we use Monte Carlo sampling to choose 2048 grid points under Gaussian distribution $\mathcal{N}(0, 0.1)$ during training. We choose $m_1 = 4$, $m_2 = 1$, and $\delta = 0.01$ as the parameters of Equation 3.

Our network is implemented with TensorFlow. We use the Adam optimizer with a learning rate of 1×10^{-4} and a batch size of 16.

For testing, we first use the camera pose prediction network to estimate the camera parameters for the input image and feed the estimated parameters as input to SDF prediction. We follow the aforementioned surface reconstruction procedure (Section 3.2) to generate the output mesh.

Evaluation Metrics For quantitative evaluations, we apply three commonly used metrics to compute the difference between a reconstructed mesh object and its ground truth mesh: (1) Chamfer Distance (CD) and (2) Earth Mover’s Distance (EMD) between uniformly sampled point clouds, and (3) Intersection over Union (IoU) on voxelized meshes. The definitions of CD and EMD can be found in the supplementary.

4.1 Single-view Reconstruction Comparison With State-of-the-art Methods

In this section, we compare our approach on single-view reconstruction with state-of-the-art methods: AtlasNet [7], Pixel2Mesh [21], 3DN [23], OccNet [12] and IMNET [2]. AtlasNet [7] and Pixel2Mesh [21] generate a fixed-topology mesh from a 2D image. 3DN [23] deforms a given source mesh to reconstruct the target model. When comparing to this method, we choose a source mesh from a given set of templates by querying a template embedding as proposed in the original work. IMNET [2] and OccNet [12] both predict the sign of SDF to reconstruct 3D shapes. Since IMNET trains an individual model for each category, we implement their model following the original paper, and train a single model on all 13 categories. Due to mismatch between the scales of shapes reconstructed by our method and OccNet, we only report their IoU, which is scale-invariant. In addition, we train a 3D CNN model, denoted by ‘3DCNN’, where the encoder is the same as DISN and a decoder is a volumetric 3D CNN structure with an output dimension of 64^3 . The ground truth for 3DCNN is the SDF values on all 64^3 grid locations. For both IMNET and 3DCNN, we use the same surface reconstruction method as ours to output reconstructed meshes. We also report the results of DISN using estimated camera poses and ground truth poses, denoted by ‘Ours_{cam}’ and ‘Ours’ respectively. AtlasNet, Pixel2Mesh and 3DN use explicit surface generation, while 3DCNN, IMNET, OccNet and our methods reconstruct implicit surfaces.

As shown in Table 1, DISN outperforms all other models in EMD and IoU. Only 3DN performs better than our model on CD, however 3DN requires more information than ours in the form of a source mesh as input. Figure 7 shows qualitative results. As illustrated in both quantitative and qualitative results, implicit surface representation provides a flexible method of generating topology-variant 3D meshes. Comparisons to 3D CNN show that predicting SDF values for given points produces smoother surfaces than generating a fixed 3D volume using an image embedding. We speculate that this is due to SDF being a continuous function with respect to point locations. It is harder for a deep network to approximate an overall SDF volume with global image features only. Moreover, our method outperforms IMNET and OccNet in terms of recovering shape details. For example, in Figure 7, local feature extraction enables our method to generate different patterns of the chair backs in the first three rows, while other methods fail to capture such details. We further validate the effectiveness of our local feature extraction module in Section 4.3. Although using ground truth camera poses (i.e., ‘Ours’) outperforms using predicted camera poses (i.e., ‘Ours_{cam}’) in quantitative results, respective qualitative results demonstrate no significant difference.

4.2 Camera Pose Estimation

We compare our camera pose estimation with [9]. Given a point cloud PC_w in world coordinates for an input image, we transform PC_w using the predicted camera pose and compute the mean distance d_{3D} between the transformed point cloud and the ground truth point cloud in camera space. We also compute the 2D reprojection error d_{2D} of the transformed point cloud after we project it onto the input image. Table 2 reports

	[9]	Ours
d_{3D}	0.073	0.047
d_{2D}	4.86	2.95

Table 2: Camera pose estimation comparison. The unit of d_{2D} is pixel.

		plane	bench	box	car	chair	display	lamp	speaker	rifle	sofa	table	phone	boat	Mean
EMD	AtlasNet	3.39	3.22	3.36	3.72	3.86	3.12	5.29	3.75	3.35	3.14	3.98	3.19	4.39	3.67
	Pixel2mesh	2.98	2.58	3.44	3.43	3.52	2.92	5.15	3.56	3.04	2.70	3.52	2.66	3.94	3.34
	3DN	3.30	2.98	3.21	3.28	4.45	3.91	3.99	4.47	2.78	3.31	3.94	2.70	3.92	3.56
	IMNET	2.90	2.80	3.14	2.73	3.01	2.81	5.85	3.80	2.65	2.71	3.39	2.14	2.75	3.13
	3D CNN	3.36	2.90	3.06	2.52	3.01	2.85	4.73	3.35	2.71	2.60	3.09	2.10	2.67	3.00
	Ours _{cam}	2.67	2.48	3.04	2.67	2.67	2.73	4.38	3.47	2.30	2.62	3.11	2.06	2.77	2.84
	Ours	2.45	2.41	2.99	2.52	2.62	2.63	4.11	3.37	1.93	2.55	3.07	2.00	2.55	2.71
CD	AtlasNet	5.98	6.98	13.76	17.04	13.21	7.18	38.21	15.96	4.59	8.29	18.08	6.35	15.85	13.19
	Pixel2mesh	6.10	6.20	12.11	13.45	11.13	6.39	31.41	14.52	4.51	6.54	15.61	6.04	12.66	11.28
	3DN	6.75	7.96	8.34	7.09	17.53	8.35	12.79	17.28	3.26	8.27	14.05	5.18	10.20	9.77
	IMNET	12.65	15.10	11.39	8.86	11.27	13.77	63.84	21.83	8.73	10.30	17.82	7.06	13.25	16.61
	3D CNN	10.47	10.94	10.40	5.26	11.15	11.78	35.97	17.97	6.80	9.76	13.35	6.30	9.80	12.30
	Ours _{cam}	9.96	8.98	10.19	5.39	7.71	10.23	25.76	17.90	5.58	9.16	13.59	6.40	11.91	10.98
	Ours	9.01	8.32	9.98	4.92	7.54	9.58	22.73	16.70	4.36	8.71	13.29	6.21	10.87	10.17
IoU	AtlasNet	39.2	34.2	20.7	22.0	25.7	36.4	21.3	23.2	45.3	27.9	23.3	42.5	28.1	30.0
	Pixel2mesh	51.5	40.7	43.4	50.1	40.2	55.9	29.1	52.3	50.9	60.0	31.2	69.4	40.1	47.3
	3DN	54.3	39.8	49.4	59.4	34.4	47.2	35.4	45.3	57.6	60.7	31.3	71.4	46.4	48.7
	IMNET	55.4	49.5	51.5	74.5	52.2	56.2	29.6	52.6	52.3	64.1	45.0	70.9	56.6	54.6
	3D CNN	50.6	44.3	52.3	76.9	52.6	51.5	36.2	58.0	50.5	67.2	50.3	70.9	57.4	55.3
	OccNet	54.7	45.2	73.2	73.1	50.2	47.9	37.0	65.3	45.8	67.1	50.6	70.9	52.1	56.4
	Ours _{cam}	57.5	52.9	52.3	74.3	54.3	56.4	34.7	54.9	59.2	65.9	47.9	72.9	55.9	56.9
	Ours	61.7	54.2	53.1	77.0	54.9	57.7	39.7	55.9	68.0	67.1	48.9	73.6	60.2	59.4

Table 1: Quantitative results on ShapeNet Core for various methods. Metrics are CD ($\times 0.001$, the smaller the better), EMD ($\times 100$, the smaller the better) and IoU (% , the larger the better). CD and EMD are computed on 2048 points.

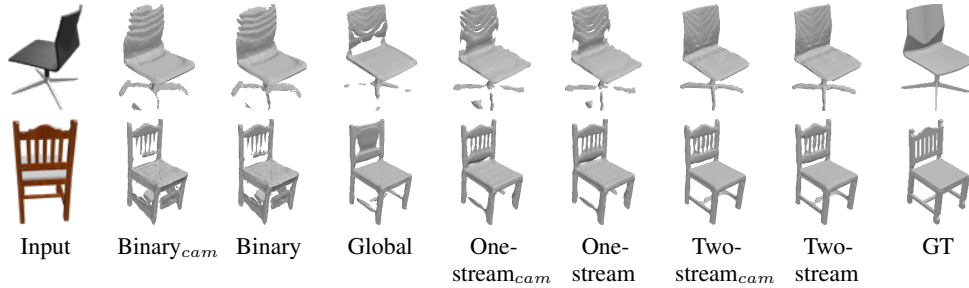


Figure 8: Qualitative results of our method using different settings. ‘GT’ denotes ground truth shapes, and ‘_{cam}’ denotes models with estimated camera parameters.

d_{3D} and d_{2D} of [9] and our method. With the help of the $6D$ rotation representation, our method outperforms [9] by 2 pixels in terms of 2D reprojection error.

4.3 Ablation Studies

To show the impact of the camera pose estimation, local feature extraction, and different network architectures, we conduct ablation studies on the ShapeNet “chair” category, since it has the greatest variety. Table 3 reports the quantitative results and Figure 8 shows the qualitative results.

Camera Pose Estimation As is shown in Section 4.2, camera pose estimation potentially introduces uncertainty to the local feature extraction process with an average reprojection error of 2.95 pixels. Although the quantitative reconstruction results with ground truth camera parameters are constantly superior to the results with estimated parameters in Table 3, Figure 8 demonstrates that a small difference in the image projection does not affect the reconstruction quality significantly.

Binary Classification Previous studies [12, 2] formulate SDF prediction as a binary classification problem by predicting the probability of a point being inside or outside the surface S_0 . Even though Section 4.1 illustrates our superior performance over [12, 2], we further validate the effectiveness of our regression supervision by comparing with classification supervision using our own network structure. Instead of producing a SDF value, we train our network with classification supervision and output the probability of a point being inside the mesh surface. We use a softmax cross entropy loss to optimize this network. We report the result of this classification network as ‘Binary’.

Local Feature Extraction Local image features of each point provide access to the corresponding local information that capture shape details. To validate the effectiveness of this information, we remove the ‘local features extraction’ module from DISN and denote this setting by ‘Global’. This model predicts the SDF value solely based on the global image features. By comparing ‘Global’ with other methods in Table 3 and Figure 8, we conclude that local feature extraction helps the model capture shape details and improve the reconstruction quality by a large margin.

Network Structures To further assess the impact of different network architectures, in addition to our original architecture with two decoders (which we call ‘Two-stream’), we also introduce a ‘One-stream’ architecture where the global features, the local features and the point features are concatenated and fed into a single decoder which predicts the SDF value. Detailed structure of this architecture can be found in the supplementary. As illustrated in Table 3 and Figure 8, the original Two-stream setting is slightly superior to One-stream, which shows that DISN is robust to different network architectures.

Camera Pose	Binary	Global	One-stream	Two-stream
	ground truth estimated	n/a	ground truth estimated	ground truth estimated
EMD	2.88 2.99	2.75 n/a	2.74 2.71	2.62 2.65
CD	8.27 8.80	7.64 n/a	8.30 7.86	7.55 7.63
IoU	54.9 53.5	54.8 n/a	53.5 53.6	55.3 53.9

Table 3: Quantitative results on the category ‘chair’. CD ($\times 0.001$), EMD ($\times 100$) and IoU (%).

4.4 Applications

Shape interpolation Figure 9 shows shape interpolation results where we interpolate both global and local image features going from the leftmost sample to the rightmost. We see that the generated shape is gradually transformed.

Test with online product images Figure 10 illustrates 3D reconstruction results by DISN on online product images. Note that our model is trained on rendered images, this experiment validates the domain transferability of DISN.



Figure 10: Test our model on online product images.



Figure 9: Shape interpolation result.

Multi-view reconstruction Our model can also take multiple 2D views of the same object as input. After extracting the global and the local image features for each view, we apply max pooling and use the resulting features as input to each decoder. We have retrained our network for 3 input views and visualize some results in Figure 11. Combining multi-view features helps DISN to further address shape details.

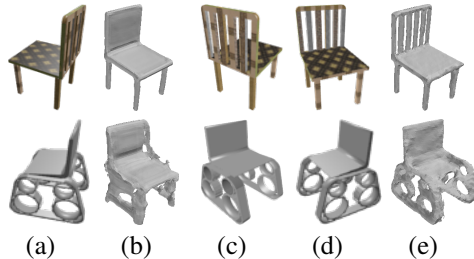


Figure 11: Multi-view reconstruction results. (a) Single-view input. (b) Reconstruction result from (a). (c)&(d) Two other views. (e) Multi-view reconstruction result from (a), (c) and (d).

5 Conclusion

In this paper, we present DISN, a deep implicit surface network for single-view reconstruction. Given a 3D point and an input image, DISN predicts the SDF value for the point. We introduce a local feature extraction module by projecting the 3D point onto the image plane with an estimated camera pose. With the help of such local features, DISN is able to capture fine-grained details and generate high-quality 3D models. Qualitative and quantitative experiments validate the superior performance of DISN over state-of-the-art methods and the flexibility of our model.

Though we achieve state-of-the-art performance in single-view reconstruction, our method is only able to handle objects with clear background since

it's trained with rendered images. To address this limitation, our future work includes extending SDF generation with texture prediction using a differentiable renderer [10].

References

- [1] A. X. Chang, T. Funkhouser, L. Guibas, P. Hanrahan, Q. Huang, Z. Li, S. Savarese, M. Savva, S. Song, H. Su, J. Xiao, L. Yi, and F. Yu. Shapenet: An information-rich 3d model repository. *arxiv*, 2015.
- [2] Z. Chen and H. Zhang. Learning implicit fields for generative shape modeling. *arXiv preprint arXiv:1812.02822*, 2018.
- [3] C. B. Choy, D. Xu, J. Gwak, K. Chen, and S. Savarese. 3d-r2n2: A unified approach for single and multi-view 3d object reconstruction. In *ECCV*, 2016.
- [4] A. Dai, C. R. Qi, and M. Nießner. Shape completion using 3d-encoder-predictor cnns and shape synthesis. In *CVPR*, 2017.
- [5] H. Fan, H. Su, and L. J. Guibas. A point set generation network for 3d object reconstruction from a single image. In *CVPR*, 2017.
- [6] R. Girdhar, D. Fouhey, M. Rodriguez, and A. Gupta. Learning a predictable and generative vector representation for objects. In *ECCV*, 2016.
- [7] T. Groueix, M. Fisher, V. G. Kim, B. Russell, and M. Aubry. AtlasNet: A Papier-Mâché Approach to Learning 3D Surface Generation. In *CVPR*, 2018.
- [8] C. Häne, S. Tulsiani, and J. Malik. Hierarchical surface prediction for 3d object reconstruction. In *3DV*, 2017.
- [9] E. Insafutdinov and A. Dosovitskiy. Unsupervised learning of shape and pose with differentiable point clouds. In *NeurIPS*, 2018.
- [10] H. Kato, Y. Ushiku, and T. Harada. Neural 3d mesh renderer. In *CVPR*, 2018.
- [11] W. E. Lorensen and H. E. Cline. Marching cubes: A high resolution 3d surface construction algorithm. In *ACM siggraph computer graphics*, 1987.
- [12] L. Mescheder, M. Oechsle, M. Niemeyer, S. Nowozin, and A. Geiger. Occupancy networks: Learning 3d reconstruction in function space. In *CVPR*, 2019.
- [13] C. Niu, J. Li, and K. Xu. Im2struct: Recovering 3d shape structure from a single rgb image. In *CVPR*, 2018.
- [14] J. J. Park, P. Florence, J. Straub, R. Newcombe, and S. Lovegrove. DeepSDF: Learning continuous signed distance functions for shape representation. *arXiv preprint arXiv:1901.05103*, 2019.
- [15] K. Simonyan and A. Zisserman. Very deep convolutional networks for large-scale image recognition. *arXiv preprint arXiv:1409.1556*, 2014.
- [16] F. S. Sin, D. Schroeder, and J. Barbič. Vega: non-linear fem deformable object simulator. In *Computer Graphics Forum*, 2013.
- [17] A. Sinha, A. Unmesh, Q. Huang, and K. Ramani. Surfnet: Generating 3d shape surfaces using deep residual networks. In *CVPR*, 2018.
- [18] J. Tang, X. Han, J. Pan, K. Jia, and X. Tong. A skeleton-bridged deep learning approach for generating meshes of complex topologies from single rgb images. In *CVPR*, 2019.
- [19] M. Tatarchenko, A. Dosovitskiy, and T. Brox. Octree generating networks: Efficient convolutional architectures for high-resolution 3d outputs. In *ICCV*, 2017.
- [20] S. Tulsiani, T. Zhou, A. A. Efros, and J. Malik. Multi-view supervision for single-view reconstruction via differentiable ray consistency. In *CVPR*, 2017.
- [21] N. Wang, Y. Zhang, Z. Li, Y. Fu, W. Liu, and Y.-G. Jiang. Pixel2mesh: Generating 3d mesh models from single rgb images. *arXiv preprint arXiv:1804.01654*, 2018.
- [22] P.-S. Wang, C.-Y. Sun, Y. Liu, and X. Tong. Adaptive o-cnn: A patch-based deep representation of 3d shapes. *arXiv preprint arXiv:1809.07917*, 2018.
- [23] W. Wang, D. Ceylan, R. Mech, and U. Neumann. 3dn: 3d deformation network. In *CVPR*, 2019.

- [24] W. Wang, Q. Huang, S. You, C. Yang, and U. Neumann. Shape inpainting using 3d generative adversarial network and recurrent convolutional networks. In *ICCV*, 2017.
- [25] J. Wu, Y. Wang, T. Xue, X. Sun, W. T. Freeman, and J. B. Tenenbaum. MarrNet: 3D Shape Reconstruction via 2.5D Sketches. In *NeurIPS*, 2017.
- [26] J. Wu, C. Zhang, X. Zhang, Z. Zhang, W. T. Freeman, and J. B. Tenenbaum. Learning shape priors for single-view 3d completion and reconstruction. In *NeurIPS*, 2018.
- [27] H. Xu and J. Barbič. Signed distance fields for polygon soup meshes. In *Proceedings of Graphics Interface 2014*, pages 35–41. Canadian Information Processing Society, 2014.
- [28] X. Yan, J. Yang, E. Yumer, Y. Guo, and H. Lee. Perspective transformer nets: Learning single-view 3d object reconstruction without 3d supervision. In *NeurIPS*, 2016.
- [29] G. Yang, Y. Cui, S. Belongie, and B. Hariharan. Learning single-view 3d reconstruction with limited pose supervision. In *ECCV*, 2018.
- [30] Y. Zhou, C. Barnes, J. Lu, J. Yang, and H. Li. On the continuity of rotation representations in neural networks. *arXiv preprint arXiv:1812.07035*, 2018.
- [31] R. Zhu, H. Kiani Galoogahi, C. Wang, and S. Lucey. Rethinking reprojection: Closing the loop for pose-aware shape reconstruction from a single image. In *ICCV*, 2017.
- [32] C. Zou, E. Yumer, J. Yang, D. Ceylan, and D. Hoiem. 3d-prnn: Generating shape primitives with recurrent neural networks. In *ICCV*, 2017.